PAPER

EDOT–diketopyrrolopyrrole copolymers for polymer solar cells†

Chao Wang,[a] Christian J. Mueller,[b] Eliot Gann,[ac] Amelia C. Y. Liu,[d] Mukundan Thelakkat[b] and Christopher R. McNeill*[a]

The photovoltaic properties of a series of diketopyrrolo[3,4-c]pyrrole (DPP) copolymers containing 3,4-ethylenedioxythiophene (EDOT) as a comonomer are reported. With use of different aryl flanking units on the DPP core, namely thiophene, pyridine or phenyl, optical gaps ranging from 1.91 eV to 1.13 eV are achieved. When blended with the fullerene derivative [6,6]-phenyl C_{71}-butyric acid methyl ester ($PC_{71}BM$), the thiophene-flanked copolymer **PDPP[T]$_2$-EDOT** with an optical gap of 1.13 eV was found to have the best photovoltaic performance, with an efficiency of 2.5% in an inverted device architecture. Despite having the lowest open circuit voltage of the three polymers studied, **PDPP[T]$_2$-EDOT**-based devices were able to achieve superior efficiencies due to the high short circuit current of up to ~15 mA cm^{-2}. **PDPP[T]$_2$-EDOT**-based devices also exhibit higher external quantum efficiencies which are associated with a superior microstructure – as revealed by transmission electron microscopy (TEM) and grazing incidence wide-angle X-ray scattering (GIWAXS) – which is associated with the enhanced aggregation tendency of **PDPP[T]$_2$-EDOT** chains. In particular **PDPP[T]$_2$-EDOT** : $PC_{71}BM$ blends were found to have a finer phase separated morphology with superior thin-film crystallinity. Surface morphology was also investigated with atomic force microscopy and near-edge X-ray absorption fine-structure spectroscopy.

(A) Introduction

Harnessing solar energy is a promising way to meet the world's rapidly increasing energy demand. Intensive research has been conducted on organic photovoltaic technologies (OPV) over the past two decades since the first demonstration of a donor/acceptor bilayer planar heterojunction in 1979.[1,2] OPVs offer several advantages compared to conventional solar technologies including solution processability, low cost, flexible substrates, semitransparency and ease of fabrication. The bilayer heterojunction architecture has certain limitations including a limited donor–acceptor interfacial area and the requirement of long exciton diffusion lengths in order to ensure sufficient exciton dissociation. Excitons in most organic semiconductors have very short lifetimes with associated diffusion lengths of about 4–20 nm,[3,4] and thus only excitons within an exciton diffusion length of the donor–acceptor interface are able to dissociate into free charges before recombining. The

bulk heterojunction (BHJ) architecture was a breakthrough for the organic photovoltaics field, greatly enhancing the yield of dissociated excitons through the forming of a nano-scale donor–acceptor morphology that evolves during the spin coating of a blend solution.[5–7] Through the development of techniques to control morphology either during or post film deposition and the development of high materials with improved light absorption and charge transporting properties, OPV devices have achieved efficiencies above 10%.[8–10]

The development of OPV technology has gone hand-in-hand with the innovation of new materials. The power conversion efficiency of organic solar cells is a product of open-circuit voltage (V_{OC}), short-circuit current (J_{SC}) and fill factor (FF). The highest occupied molecular orbital (HOMO) level of the electron donor material and the lowest unoccupied molecular orbital (LUMO) level of the electron acceptor material roughly determine the maximum achievable V_{OC}, while the lowest optical gap (E_g) of the two materials largely determines maximum possible J_{SC}.[11] With regard to polymer donors, the key issues of polymer design include engineering the band gap and energy levels to achieve high J_{SC} and V_{OC}. In an ideal case, a low band-gap polymer, whose absorption extends into the inferred region, can greatly improve the J_{SC} as more photons can be converted to electrons. Thus fine tuning of HOMO and LUMO levels is required to achieve a high V_{OC} with a small band gap, while maintaining a LUMO level high enough for efficient charge separation.[12] In addition, high performance polymeric donor materials should possess high

[a]*Department of Materials Science and Engineering, Monash University, Wellington Road, Clayton, VIC 3800, Australia. E-mail: christopher.mcneill@monash.edu*

[b]*Applied Functional Polymers, Macromolecular Chemistry I, University of Bayreuth, 95440 Bayreuth, Germany*

[c]*Australian Synchrotron, 800 Blackburn Road, Clayton, VIC 3168, Australia*

[d]*Monash Centre for Electron Microscopy and School of Physics, Monash University, Clayton, Victoria 3800, Australia*

† Electronic supplementary information (ESI) available. See DOI: 10.1039/c5ta10078j

This journal is © The Royal Society of Chemistry 2016

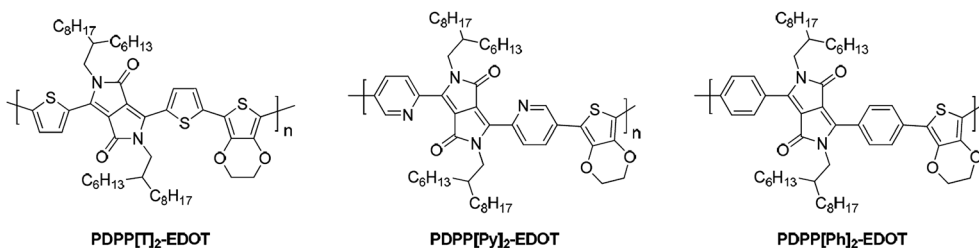*J. Mater. Chem. A*, 2016, 4, 3477–3486 | **3477**

Fig. 1 Chemical structures of PDPP[T]₂-EDOT, PDPP[Py]₂-EDOT and PDPP[Ph]₂-EDOT.

hole mobilities and the ability to be processed with a suitable acceptor to form an optimal phase-separated morphology.

The recent success of polymer/fullerene solar cells that utilise a polymeric donor and fullerene acceptor has resulted largely from the development of new low band-gap donor materials. The donor–acceptor design, where electron rich and electron deficient units alternate along the copolymer backbone is commonly used to tune the HOMO and LUMO energy levels and the optical gap of these polymers.[13] While many different building blocks have been utilised for the construction of donor–acceptor copolymers, the electron deficient diketopyrrolopyrrole (DPP) unit has proved to be a versatile acceptor unit with DPP-based copolymers possessing low band gaps for polymer solar cell applications[14,15] and high carrier mobilities in field-effect transistors.[16] In particular power conversion efficiencies of up to 9.4% have been achieved,[17–19] with bandgaps as low as 1.13 eV also realised for DPP-based polymers.[20] It is the strong electron deficient character of the DPP moiety, combined with high planarity and aggregation, that allows these novel materials to absorb in the near infrared region and exhibit good electron and hole mobilities.[16]

Here we report the photovoltaic properties of novel DPP-based copolymers that incorporate the electron rich 3,4-ethylenedioxythiophene (EDOT) as comonomer with different aryl flanking units on either side of the DPP core, see Fig. 1.[21] The use of EDOT as a comonomer is motivated by its strong electron rich character which can enhance the p-type character of PDPP materials and provide non-covalent, diffusive H···O interactions to the adjacent aryl units in the backbone.[19] Through the use of different flanking units, tuning of the bandgap is achieved with an optical bandgap as low as 1.13 eV achieved with the use of thiophene flanking units which promote a more coplanar backbone. Interestingly, the highest efficiencies are achieved with the lowest bandgap material that exhibits a broad spectral response from 350 nm to over 1000 nm. As well as characterising the performance of these novel polymers in inverted and standard device configurations, the microstructure of blends with the fullerene derivative [6,6]-phenyl C₇₁-butyric acid methyl ester (PC₇₁BM) are also reported.

(B)   Result and discussion

Materials

Fig. 1 presents the chemical structures of the three DPP–EDOT polymers investigated. These three polymers employ the DPP moiety as the electron deficient unit along with the EDOT unit as an electron rich comonomer. For the polymer PDPP[T]₂-EDOT, thiophene units are used as flanking units either side of the DPP moiety. For the polymer PDPP[Py]₂-EDOT pyridine units are used as flanking units while for PDPP[Ph]₂-EDOT phenyl units are used as flanking units. The synthesis of these materials has been reported separately.[21] The electrochemical and optoelectronic properties are strongly influenced by the choice of flanking unit, with the HOMO, LUMO and bandgap values of these polymers summarised in Table 1. The low band gap of the thiophene containing polymer is attributed not only to the planar structure of the polymer backbone but also to a very strong push–pull effect of the electron rich EDOT and the electron deficient DPP core.[21] Table 1 also summarises the molecular weights of the polymers with a number average molecular weight (M_n) of 142 kg mol^{-1} for PDPP[T]₂-EDOT, $M_n = 25.7$ kg mol^{-1} for PDPP[Py]₂-EDOT and $M_n = 16.7$ kg mol^{-1} for PDPP[Ph]₂-EDOT. With variation of the choice of flanking unit, tuning of the bandgap is achieved with an optical gap (E_{opt} determined from absorption onset in film[21]) of 1.13 eV for PDPP[T]₂-EDOT, $E_{opt} = 1.59$ eV for PDPP[Py]₂-EDOT and $E_{opt} = 1.91$ eV for PDPP[Ph]₂-EDOT.

Optical properties

Fig. 2 presents the normalized optical absorption spectra of blended films of PDPP[T]₂-EDOT : PC₇₁BM, PDPP[Py]₂-EDOT : PC₇₁BM and PDPP[Ph]₂-EDOT : PC₇₁BM. These blends were are all spin-coated from chloroform solutions with 2 vol% of DIO additive and a weight ratio of 1 : 2 polymer : fullerene. Both polymer and fullerene components contribute to the absorption spectrum of the blend film, with PC₇₁BM contributing at wavelengths lower than 600 nm and a distinct peak in the visible at around 465 nm and further peaks in the UV range. The absorption onsets of the polymers vary from 650 nm for PDPP[Ph]₂-EDOT to 780 nm for PDPP[Py]₂-EDOT and extend out to 1100 nm for PDPP[T]₂-EDOT, matching the absorption features previously seen in neat polymer films.[21] The high band gap PDPP[Ph]₂-EDOT has a relatively narrow absorption range with only one distinct peak at 550 nm, with the lack of vibronic features attributed to its low planarisation due to large dihedral angles and hence decreased delocalization.[21] The intermediate optical gap PDPP[Py]₂-EDOT : PC₇₁BM has two distinct peaks at around 640 and 710 nm consistent with vibronic features while the low band gap PDPP[T]₂-EDOT has a broad near infrared

3478 | J. Mater. Chem. A, 2016, 4, 3477–3486

This journal is © The Royal Society of Chemistry 2016

Table 1 Characteristics of PDPP[T]$_2$-EDOT, PDPP[Py]$_2$-EDOT and PDPP[Ph]$_2$-EDOT[21]

Polymer	M_n (kg mol^{-1})	$Đ$	HOMO (eV)	LUMO (eV)	E_g (eV)	E_{opt} (eV)
PDPP[T]$_2$-EDOT	142	2.7	−5.73	−3.66	2.07	1.13
PDPP[Py]$_2$-EDOT	25.7	2.4	−6.07	−3.74	2.33	1.59
PDPP[Ph]$_2$-EDOT	16.7	2.1	−5.89	−3.53	2.36	1.91
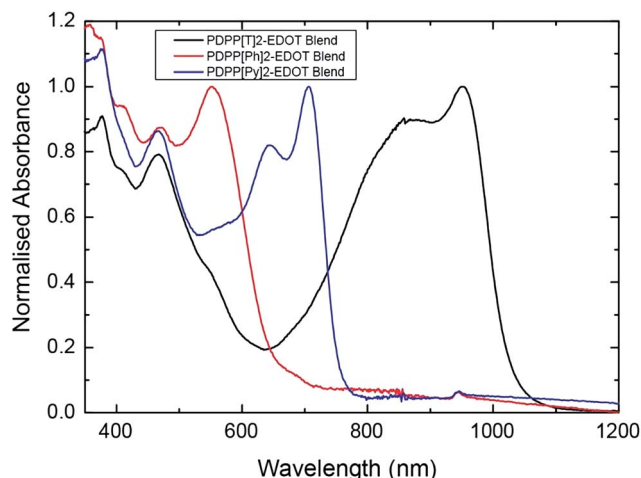
Fig. 2 Ultraviolet to near-infrared absorption spectra of blend films of PDPP[T]$_2$-EDOT : PC$_{71}$BM, PDPP[Py]$_2$-EDOT : PC$_{71}$BM and PDPP[Ph]$_2$-EDOT : PC$_{71}$BM.

absorption band ranging from 640 nm to 1100 nm with two distinct vibronic peaks at 950 and 850 nm.

Device performance

In this study, the performance of both standard and inverted devices has been evaluated. Devices with a standard structure consisted of ITO/MoO$_3$/active layer/Ca/Al, while devices based on an inverted structure consisted of ITO/ZnO/PEIE/active layer/MoO$_3$/Ag. The active layers are all spin-coated from chloroform solutions with 2 vol.% DIO with the active layer thickness separately optimised for each polymer. Details of device fabrication and testing are described in the Experimental section. Fig. 3a–d presents the current density versus voltage characteristics (J–V curves) of devices under AM1.5G simulated sunlight and in the dark for both standard and inverted structures. Device performance parameters such as J_{SC}, V_{OC}, FF and power conversion efficiency (PCE) are summarized in Table 2. In general, EDOT-polymer devices with a high band gap show a higher V_{OC} and a lower J_{SC}, while low band gap EDOT-polymer devices exhibit a higher J_{SC} and a lower V_{OC}. The standard architecture **PDPP[T]$_2$-EDOT** : PC$_{71}$BM device shows an efficiency of only 0.69% with a short circuit current of 6.8 mA cm^{-2} and an open-circuit voltage of 0.25 V. In comparison, we found significant improvement in performance for the inverted device structure for **PDPP[T]$_2$-EDOT** : PC$_{71}$BM blends with an almost 4-fold increase in efficiency to 2.5%, mainly resulting from an increase in J_{SC} to 15.5 mA cm^{-2} along with improvements in V_{OC} (an increase from 0.25 V to 0.32 V) and FF (from 0.40 to 0.50).

The standard **PDPP[Py]$_2$-EDOT** : PC$_{71}$BM device on the other hand shows a higher PCE (2.2%), compared with inverted structure device (1.4%). The J_{SC} of both types of **PDPP[Py]$_2$-EDOT** : PC$_{71}$BM devices are very similar (5.1 mA cm^{-2} versus 4.9 mA cm^{-2}), while the V_{OC} and FF of the standard structure device are both slightly higher (0.80 V versus 0.70 V and 0.54 versus 0.41 respectively). Despite a relatively high V_{OC} (0.97 V for standard and 0.91 V for inverted structure), **PDPP[Ph]$_2$-EDOT** : PC$_{71}$BM devices gave a very moderate PCE of 1.7% for both architecture devices largely due to the low J_{SC} (4.1 mA cm^{-2} for standard and 4.4 mA cm^{-2} for inverted structures).

Fig. 3c and d present the dark J–V characteristics for both standard and inverted architectures. For standard structure devices, the current leakage values of **PDPP[Py]$_2$-EDOT** : PC$_{71}$BM and **PDPP[Ph]$_2$-EDOT** : PC$_{71}$BM devices are about 2 orders of magnitude lower than that of the **PDPP[T]$_2$-EDOT** : PC$_{71}$BM device, with the high leakage of standard **PDPP[T]$_2$-EDOT** : PC$_{71}$BM device likely affecting the FF of this device. In comparison, for the inverted structure, the dark current value of the **PDPP[T]$_2$-EDOT** device is strongly suppressed, and is one order of magnitude lower than that of the **PDPP[Py]$_2$-EDOT** device.

The external quantum efficiency (EQE) curves of devices are presented in Fig. 3e and f, which agree well with the reported J_{SC} values. The low band gap **PDPP[T]$_2$-EDOT** : PC$_{71}$BM device based on an inverted structure has a broad photo-response from 350 nm to over 1000 nm with the highest EQE value of 51.6% at 415 nm. Despite the lower band gap of **PDPP[T]$_2$-EDOT**, the inverted **PDPP[T]$_2$-EDOT** : PC$_{71}$BM still has higher EQE values than the inverted devices based on the other two polymers. In the standard configuration, the peak EQE is highest for the highest band gap material, with the **PDPP[T]$_2$-EDOT** : PC$_{71}$BM device having the lowest peak EQE. The fact that the peak EQE values are generally less than 50% (and below 30% for the case of (**PDPP[Py]$_2$-EDOT** and **PDPP[Ph]$_2$-EDOT**)) indicates that the relatively low efficiencies of these cells compared to current high performance systems are due to relatively low quantum efficiency of charge collection.

Morphology

In order to understand the relationship between the device performance, morphology, and chemical structure, the microstructure of these PDPP–EDOT copolymer : fullerene blends have been probed with a series of characterization techniques. Atomic force microscopy (AFM) was used to image the surface features while transmission electron microscopy (TEM) was employed to image the bulk morphology. Synchrotron-based grazing incidence wide-angle X-ray scattering (GIWAXS) was employed to study thin-film crystallinity with near-edge X-ray
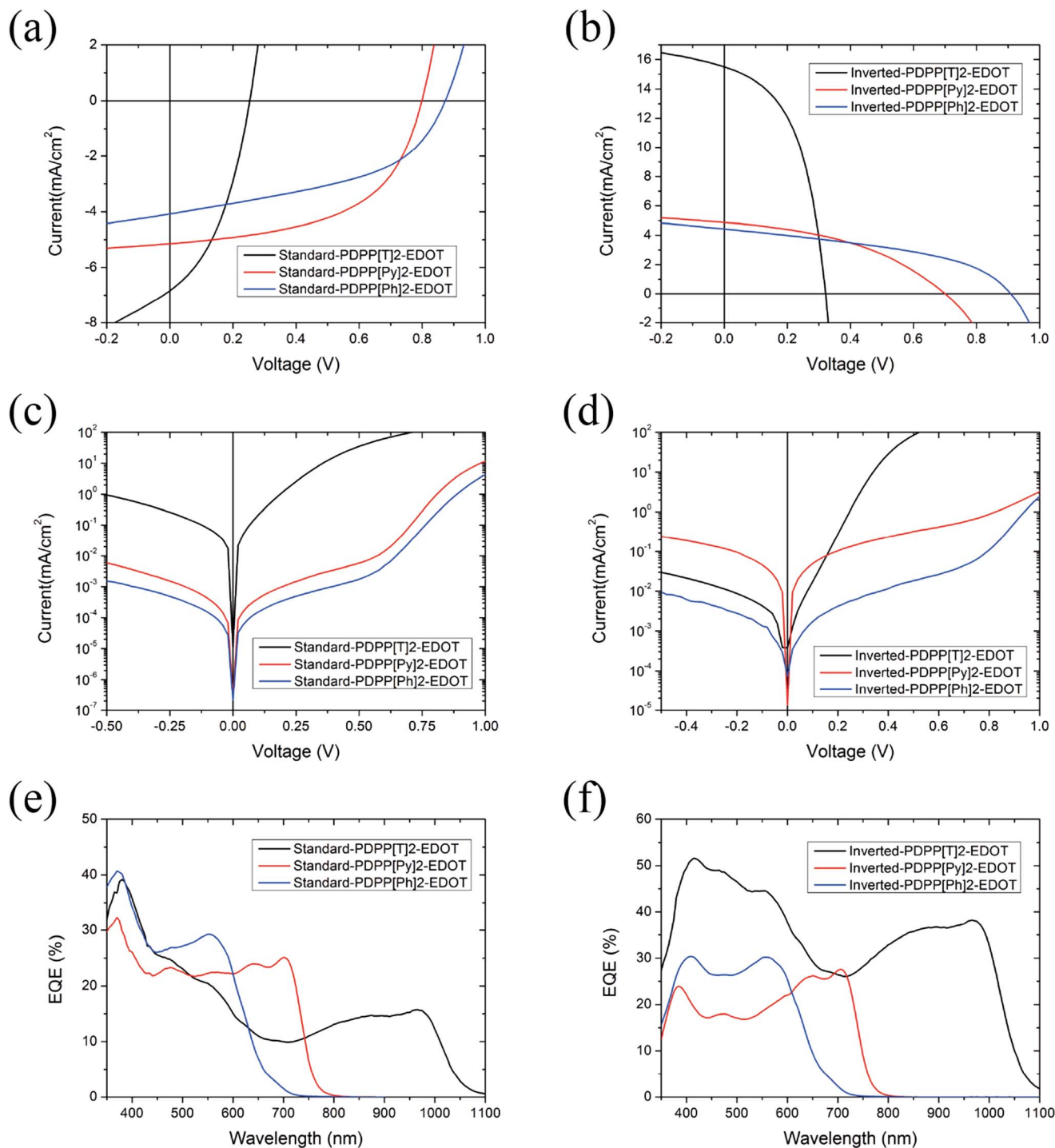
Fig. 3 Device performance of standard (ITO/MoO$_3$/active layer/Ca/Al) and inverted (ITO/ZnO/PEIE/active layer/MoO$_3$/Ag) devices with **PDPP[T]$_2$-EDOT** : PC$_{71}$BM, **PDPP[Py]$_2$-EDOT** : PC$_{71}$BM and **PDPP[Ph]$_2$-EDOT** : PC$_{71}$BM active layers: (a and b) *J–V* curves under 100 mW cm^{-2} AM 1.5G simulated sunlight, (c and d) *J–V* curves taken in the dark, (e and f) external quantum efficiency (EQE) curves.

absorption fine structure (NEXAFS) spectroscopy also used to assess surface composition.

    AFM and TEM. The AFM surface topography (a, c and e) and TEM micrographs (b, d and f) are shown in Fig. 4. The films for TEM and AFM analysis were prepared under the same condition as those of devices. The surface of the **PDPP[T]$_2$-EDOT** : PC$_{71}$BM film (Fig. 4a) shows a smooth surface and fibrous structures

with a surface roughness (R_q, root mean squared) value of 2.0 nm. In comparison, the surface features become larger and rougher in the **PDPP[Py]$_2$-EDOT** : PC$_{71}$BM film (Fig. 4b) with a surface roughness of R_q = 4.0 nm. A dramatic change is observed for the **PDPP[Ph]$_2$-EDOT** : PC$_{71}$BM blend, Fig. 4e, which is characterised by relatively large surface undulations with a surface roughness of R_q = 6.3 nm. The AFM images

Table 2 Device performance of both standard and inverted devices based on PDPP[T]₂-EDOT, PDPP[Py]₂-EDOT and PDPP[Ph]₂-EDOT

Device	J_{SC} (mA cm⁻²)	V_{OC} (V)	FF	PCE (%)
Standard **PDPP[T]₂-EDOT**	6.8 ± 0.3	0.25 ± 0.01	0.40 ± 0.01	0.7 ± 0.1
Standard **PDPP[Py]₂-EDOT**	5.1 ± 0.4	0.80 ± 0.01	0.54 ± 0.01	2.2 ± 0.2
Standard **PDPP[Ph]₂-EDOT**	4.1 ± 0.2	0.97 ± 0.01	0.47 ± 0.01	1.7 ± 0.1
Inverted **PDPP[T]₂-EDOT**	15.5 ± 0.2	0.32 ± 0.01	0.50 ± 0.01	2.5 ± 0.1
Inverted **PDPP[Py]₂-EDOT**	4.9 ± 0.2	0.70 ± 0.01	0.41 ± 0.01	1.4 ± 0.1
Inverted **PDPP[Ph]₂-EDOT**	4.4 ± 0.1	0.91 ± 0.01	0.43 ± 0.01	1.7 ± 0.1
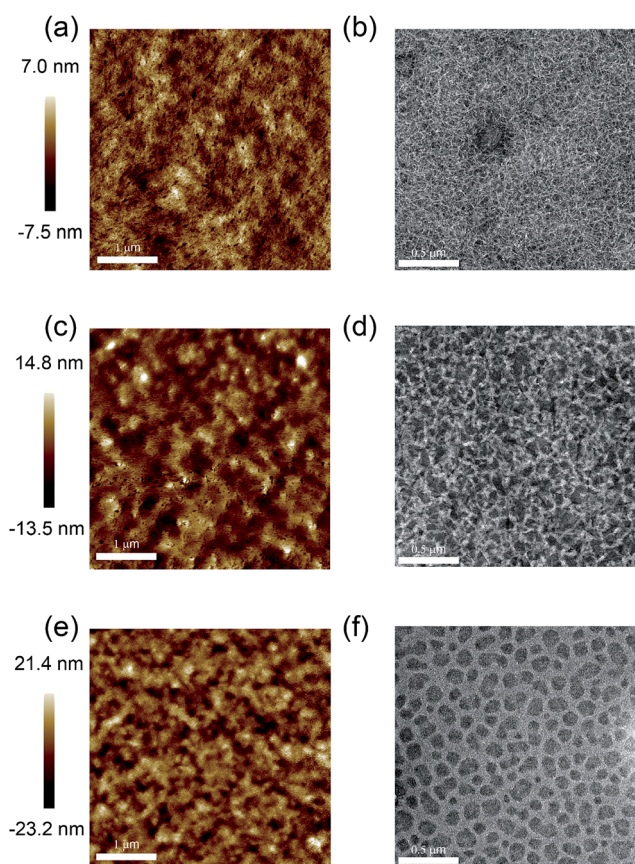
Fig. 4 AFM (a, c and e) and TEM images (b, d and f) of the **PDPP[T]₂-EDOT** : PC₇₁BM blend (a and b), **PDPP[Py]₂-EDOT** : PC₇₁BM blend (c and d), and the **PDPP[Ph]₂-EDOT** : PC₇₁BM blend (e and f).

suggest variations in the underlying morphology which are confirmed by the TEM images. For the **PDPP[T]₂-EDOT** : PC₇₁BM film (Fig. 4b) a fine continuous fibrous structure is seen indicating a relatively fine phase separated structure and consistent with the smooth surface observed with AFM. Measurement of fibril width yielded an average fibril width of 9 ± 3 nm. Some larger features are observed which are attributed to polymer aggregates and are likely associated with the higher regions seen in the AFM image. A coarser phase-separated structure is observed for the **PDPP[Py]₂-EDOT** : PC₇₁BM film (Fig. 4d) with average fibril width of 23 ± 4 nm. A different morphology is observed in TEM image of the **PDPP[Ph]₂-EDOT** : PC₇₁BM film as shown in Fig. 4f, with dark, enclosed domains of average diameter of 70 ± 10 nm surrounded by an

interconnected phase with average with of 30 ± 10 nm. Due to the higher density of the fullerene, the enclosed domain with darker contrast is likely to be fullerene-rich with the continuous phase polymer rich. The variations in thin film morphology observed by TEM go some way to explain the observed trends in device performance. Indeed, Li *et al.* have previously established a relationship between fibril width and solar cell performance in polymer : fullerene blends based on DPP polymers.[22] For the polymers investigated here, the **PDPP[T]₂-EDOT** : PC₇₁BM blend has the finest morphology with narrowest fibril width, consistent with the high EQEs achieved in inverted **PDPP[T]₂-EDOT** : PC₇₁BM devices. With increased fibril width, the **PDPP[Py]₂-EDOT** : PC₇₁BM blend has a lower maximum EQE than **PDPP[T]₂-EDOT**-based devices. Interestingly the **PDPP[Ph]₂-EDOT** : PC₇₁BM film does not have a fibrillar morphology, rather having a morphology suggestive of liquid–liquid phase separation seen in other systems such as the MDMO-PPV : PC₆₁BM and PTB7-Th : PC₇₁BM where spherical, fullerene-rich domains are surrounded by a continuous polymer-rich phase.[23,24] In PDPP : PCBM blends the use of a solvent additive such as DIO is usually effective in suppressing liquid–liquid phase separation[22,25] however for the case of the **PDPP[Ph]₂-EDOT** : PC₇₁BM blend this does not seem to be the case. van Franeker[25] have recently found that for a PDPP : PCBM blend that the presence of the solvent additive DIO induces aggregation of polymer chains suppressing liquid–liquid separation. This observation may suggest that **PDPP[Ph]₂-EDOT** chains with phenyl flanking units have a reduced tendency to aggregate, which is supported by UV-vis measurements of neat **PDPP[Ph]₂-EDOT** films[21] and of **PDPP[Ph]₂-EDOT** : PC₇₁BM blends that exhibit a lack of vibrational structure. In contrast for the more strongly aggregating **PDPP[Py]₂-EDOT** and **PDPP[T]₂-EDOT** chains fibrillar morphologies are observed resulting from the increased tendency of these chains to aggregate. Thus the choice of flanking unit not only strongly affects the optical properties of these polymers but it also strongly influences the thin-film morphologies achieved in blends with PC₇₁BM. Certainly for the case of the **PDPP[Ph]₂-EDOT** : PC₇₁BM the coarse morphology observed is limiting cell efficiency, with morphological feature much greater than the exciton diffusion length. For the **PDPP[Py]₂-EDOT** : PC₇₁BM blend the large fibril widths observed there (23 ± 4 nm) are also not optimal for cell performance. Therefore it appears that the morphologies achieved so far are limiting the overall efficiency achieved with these polymers, particularly for the **PDPP[Py]₂-EDOT** and **PDPP [Ph]₂-EDOT**-based cells. Interestingly Li *et al.*[22] also correlated

fibril width with solubility, with less soluble DPP-based polymers giving narrower fibrils. Higher molecular weight polymers also lead to a reduced solubility which in turn results in a smaller fibre width.[26] Out of the three polymers, the DPP derivatives with a six-membered ring as the aryl flanking units, *i.e.* **PDPP[Py]₂-EDOT** and **PDPP[Ph]₂-EDOT**, show a significantly lower tendency to aggregate (**PDPP[T]₂-EDOT** is also the most crystalline, see below) leading to a worse fibre network formation. Even for the highest performing **PDPP[T]₂-EDOT : PC₇₁BM** blend efficiency could be significantly increased by reducing the average fibril width from ∼10 nm to ∼5 nm (ref. 22) such as through the use of higher molecular weight samples. Thus these results highlight the importance of intermolecular interactions in determining nanoscale morphology and hence overall cell performance.

GIWAXS. Fig. 5 presents GIWAXS measurements on the PDDP-EDOT : PC₇₁BM blends assessing the thin-film crystallinity. Despite the apparent ordered fibrillar network seen in the TEM images (and similar to previous results[22]) the GIWAXS patterns indicate a low degree of crystalline ordering in the polymer phase compared to other systems such as regioregular

P3HT : fullerene films. The scattering patterns are largely dominated by the scattering of PC₇₁BM aggregates (halo at ∼1.3 Å⁻¹) though polymer scattering features can also be discerned. **PDPP [T]₂-EDOT** appears to be the most highly ordered on the 3 polymers, with a clear alkyl lamellar stacking peak observed at 0.34 Å⁻¹ consistent with previous bulk WAXS measurements on the neat polymer.[21] For the other two polymers, an alkyl lamellar stacking peak can only barely be discerned, being much broader and consistent with a significantly shorter crystalline coherence length. The peak positions of the alkyl lamellar stacking peaks for **PDPP[Py]₂-EDOT** and **PDPP[Ph]₂-EDOT** are consistent with the bulk SAXS measurements of ∼0.40 Å⁻¹ and 0.37 Å⁻¹ with the different lamellar stacking distances for the different polymers attributed to the different backbone conformations. In particular the thiophene-flanked PDPP with the highest lamellar stacking distance (∼18.4 Å) has a more coplanar conformation compared to the phenyl-flanked PDPP which has a more twisted backbone conformation and a smaller inter-lamellar distance (∼15.9 Å).

From the χ-dependence (polar angle-dependence) of the lamellar stacking peak it is possible to calculate Herman's orientational parameter, S, to quantify the orientation of
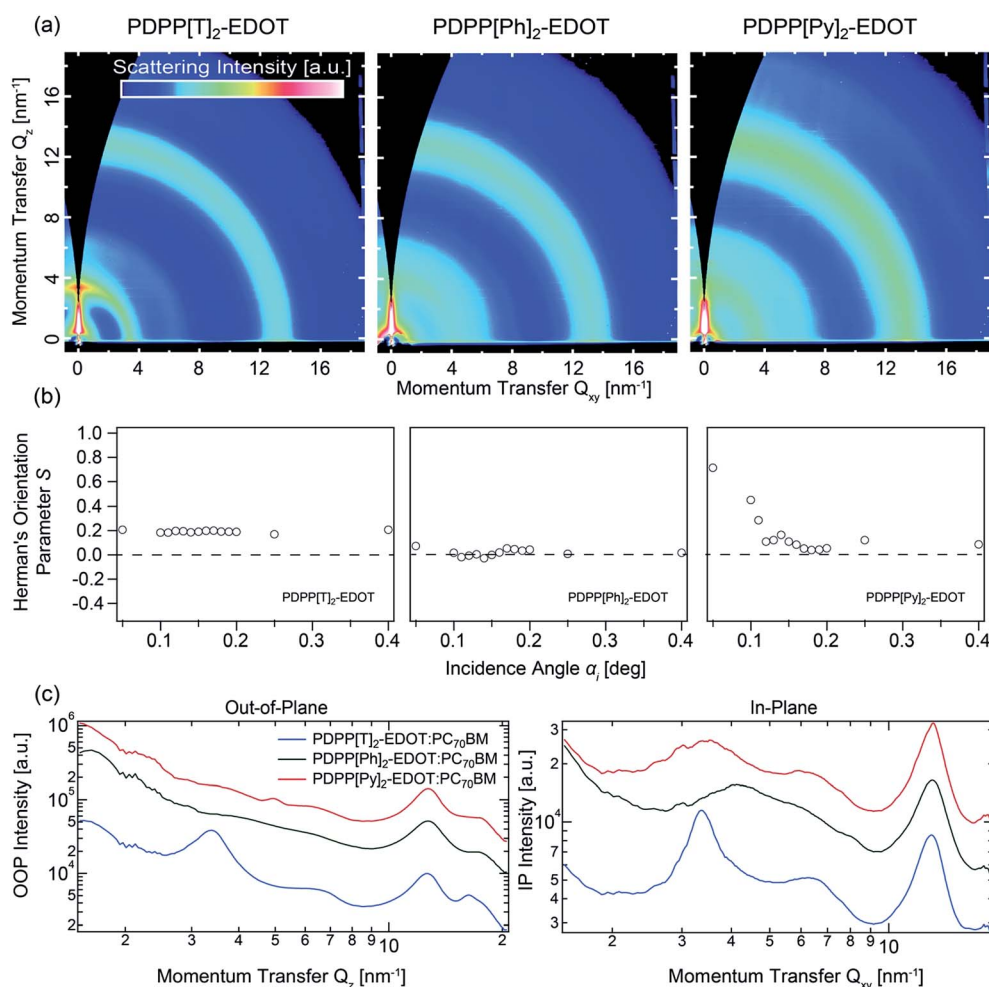

Fig. 5 GIWAXS results of the PDDP-EDOT : PC₇₁BM blends: (a) 2D scattering images, (b) plot of Herman's orientation parameter of the (100) peak *vs.* X-ray angle of incidence α, (c) out-of-plane and in-plane line profiles taken from sector cuts of the 2D images in part (a).

3482 | *J. Mater. Chem. A*, 2016, **4**, 3477–3486

This journal is © The Royal Society of Chemistry 2016

crystallites relative to the substrate.[27] The calculated values for S range from $S = -0.5$ to $S = 1$ corresponding to fully face-on or fully edge-on, respectively, with $S = 0$ indicating no preferential orientation. S is plotted as a function of X-ray angle of incidence α based on the analysis of 2D GIWAXS patterns taken at different grazing angles ranging from $\alpha = 0.05°$ to $\alpha = 0.40°$. For angles below the critical angle, identified as $\alpha_C = 0.17°$ in this case based on the angle which gives the highest scattering intensity, scattering is primarily from the top 10 nm of the film, while for angles above the critical angle X-rays scatter from throughout the film. For the **PDPP[T]$_2$-EDOT** : PC$_{71}$BM blend, a value of $S = 0.2$ is determined independent of angle of incidence indicating that the **PDPP[T]$_2$-EDOT** crystallites have a slight edge-on preference that is uniform throughout the depth of the film. For the **PDPP[Py]$_2$-EDOT** : PC$_{71}$BM blend a consistent value of $S \sim 0$ is calculated for different values of α indicating that the **PDPP[Py]$_2$-EDOT** crystallites are randomly oriented throughout the film. Finally, for the **PDPP[Ph]$_2$-EDOT** : PC$_{71}$BM blend, a strong α-dependence of S is observed, with S ranging from 0.8 at the surface (indicating a strong edge-on orientation preference) to $S = 0$ within the bulk, indicating no strong orientational preference lower in the film.

NEXAFS spectroscopy. To complement the above microstructural analyses, NEXAFS spectra were acquired of the top surface with a view to determining surface composition. Total electron yield (TEY) spectra were collected from blend films and are compared to that from neat polymer and PC$_{71}$BM films, see Fig. 6. In the TEY modality, X-ray absorption is determined by measuring the number of electrons that leave the sample *via* measurement of the drain current that flows into the sample to compensate for the lost electrons. Due to the limited mean-free-path of electrons in solids, TEY has a surface sensitivity of $\sim$3 nm,[28] providing information about the chemical composition of the top surface layer. Spectra were collected at an X-ray angle of incidence of 55° to mitigate orientational effects.[29]

By comparing the blend spectra with that of the reference neat spectra, it is clear that the blend spectra better resemble the neat polymer spectra indicating that the top surface is polymer-rich. By fitting the blend spectra to a linear combination of neat spectra it is possible to determine a %-surface composition. Interestingly, when fitting over the full spectral range the best-fit linear combination deviates from the measured blend spectrum in each case, see ESI.† This deviation is attributed to the polymer chains having a different surface conformation in the neat films compared to blends, with more side-chains exposed to the surface in the blends compared to the neat films, which changes the weighting of the spectra in the π^* and σ^* regions. To account for this discrepancy, in order to obtain reliable chemical compositions, fits have been made over (i) the entire spectral window (280 eV to 320 eV), (ii) over the π^* region (282 eV to 287 eV) and (iii) over the σ^* region (287 to 320 eV). Details of these fits can be found in the electronic ESI.† Based on these fits, the surface composition of the **PDPP[T]$_2$-EDOT** : PC$_{71}$BM blend was determined to be 78 $\pm$ 9 wt% polymer, the surface composition of the **PDPP[Py]$_2$-EDOT** : PC$_{71}$BM blend to be 92 $\pm$ 8 wt% polymer and the surface composition of the **PDPP[Ph]$_2$-EDOT** : PC$_{71}$BM blend to be 70 $\pm$ 3 wt% polymer.
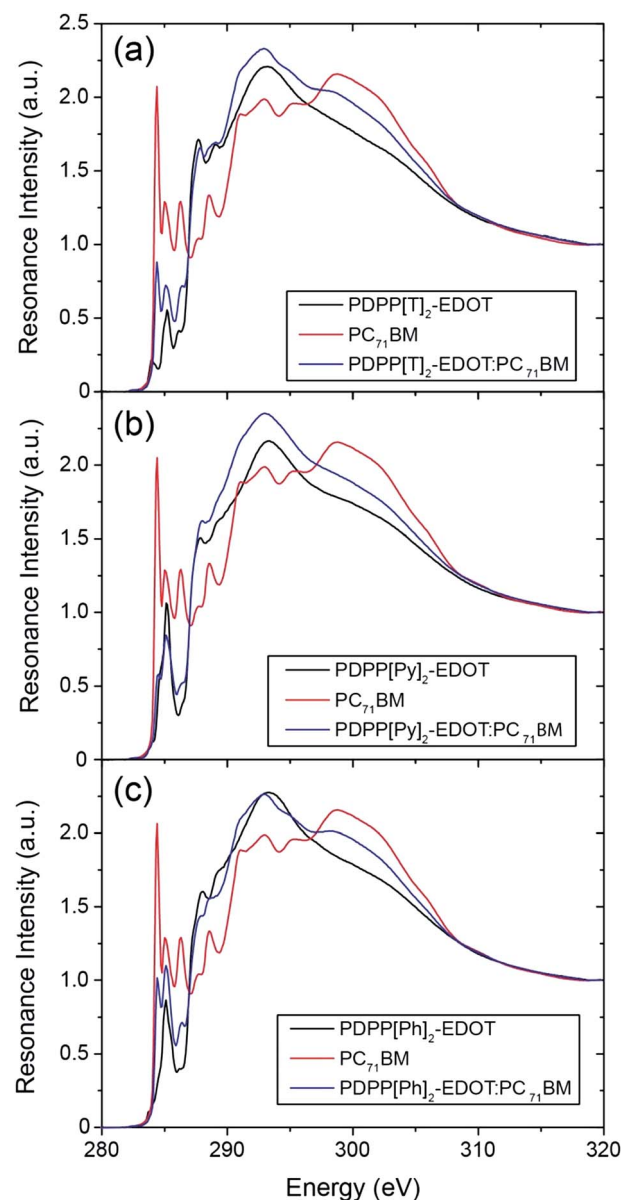

Fig. 6 Total electron yield NEXAFS spectra of the top surface of neat films and blends.

Discussion

For the series of PDPP–EDOT polymers investigated here, the polymer with thiophene flanking units achieved the highest efficiency despite having the lowest V_{OC}. The superior performance of the **PDPP[T]$_2$-EDOT**-based cells are largely due to the higher J_{SC} with the other polymers achieving higher V_{OC} and FF values. The high J_{SC} of the **PDPP[T]$_2$-EDOT**-based devices is a product of the higher EQE values obtained and the broader spectral response, with **PDPP[T]$_2$-EDOT** having an optical gap of 1.13 eV, one of the lowest band gaps reported for a DPP polymer.[20,30] While the low bandgap accounts for the broad spectral coverage, the higher EQE values for the **PDPP[T]$_2$-EDOT** : PC$_{71}$BM cells can be attributed to the more optimal morphology of **PDPP[T]$_2$-EDOT** : PC$_{71}$BM blends, with a narrower fibril width and superior crystalline structure. Furthermore, space-charge limited current

measurements of mobility in a diode configuration give a hole mobility of $\sim 3 \times 10^{-4}$ cm^2 V^{-1} s^{-1} for **PDPP[T]₂-EDOT** compared to $\sim 2 \times 10^{-6}$ cm^2 V^{-1} s^{-1} for **PDPP[Py]₂-EDOT** and $\sim 4 \times 10^{-5}$ cm^2 V^{-1} s^{-1} for **PDPP[Ph]₂-EDOT**.[21] This superior hole mobility also allows for **PDPP[T]₂-EDOT** : PC$_{71}$BM cells to have a thicker active layer thickness (~ 100 nm) compared to the other blends (~ 40 to 60 nm) that enables improved light harvesting without a severe increase in recombination. The performance of **PDPP[T]₂-EDOT**-based devices could be further improved either by better control over processing, by pairing **PDPP[T]₂-EDOT** with a more optimum acceptor that would promote a higher V_{OC}, or by improving light absorption particularly in the 600 nm to 800 nm region such as with a retroreflective foil.[31] It is also interesting to note that the **PDPP[T]₂-EDOT** : PC$_{71}$BM cells have a much higher efficiency in the inverted configuration compared to the standard device configuration. The reason for this difference is not clear, since hole and electron mobilities are expected to be relatively balanced for the **PDPP[T]₂-EDOT** and PC$_{71}$BM, though enrichment of polymer at the top surface may favour an inverted geometry. It is noted that the standard device architecture can lead to greater parasitic absorption particularly in the NIR region compared to inverted devices as observed by Hendriks et al.[20] While Hendriks et al. used PEDOT : PSS and LiF/Al layers in their standard devices, the use of a calcium electrode here will produce greater parasitic absorption compared to Al. In particular, Ca only has a maximum reflectivity of 80% over visible to NIR wavelengths[32] which will likely result in significant absorption in the top electrode. Silver electrodes in contrast act as a very efficient back reflector at NIR wavelengths. Thus careful choice of electrodes and interlayers and interlayer thicknesses must be considered with the implementation of NIR absorbing polymers.

(C) Experimental section

Materials

The synthesis of **PDPP[T]₂-EDOT**, **PDPP[Py]₂-EDOT** and **PDPP[Ph]₂-EDOT** have been reported previously.[21] PC$_{71}$BM was purchased from Nano-C, while polyethylenimine, 80% ethoxylated solution, 1,8-diiodooctane (98%) and zinc acetate dehydrate (99.999% trace metals basis) were all purchased from Sigma-Aldrich.

Device fabrication

The standard device structure employed was ITO/MoO$_x$/active layer/Ca/Al while the inverted device structure was ITO/ZnO/PEIE/active layer/MoO$_x$/Ag. For standard devices MoO$_x$ was thermally evaporated in vacuo ($\sim 10^{-6}$ mbar) onto cleaned ITO/glass with a thickness of 15 nm. For inverted devices, a 0.073 M ZnO precursor solution was prepare by dissolving 160 mg of zinc acetate dehydrate in 61 mg of ethanolamine and 10 mL of 2-methoxyethanol with vigorous stirring for 12 hours for the hydrolysis reaction at 60 °C. 0.073 M ZnO solution was then spin-coated onto cleaned ITO/glass at 3000 rpm for 30 s and annealed on hot plate at 200 °C for 30 minutes to form a thin conducting layer. Subsequently a 0.4 wt% PEIE solution was spin-coated at 5000 rpm for 30 s and annealed on hot plate at

110 °C for 15 min to form a thin hole-blocking layer. The active layers of the standard devices were all spin-coated from blend solutions at 4000 rpm for 1 min for standard devices, and 4000 rpm, 6000 rpm and 8000 rpm for 1 min for inverted **PDPP[T]₂-EDOT** : PC$_{71}$BM, **PDPP[Py]₂-EDOT** : PC$_{71}$BM and **PDPP[Ph]₂-EDOT** : PC$_{71}$BM devices respectively. The solvent employed was chloroform with 2 vol% DIO additive and total concentration of the blend solutions were all set at 12 mg mL^{-1} with a PDPP–EDOT : PC$_{71}$BM ratio of 1 : 2. The average active layer thickness were 96 nm, 68 nm and 65 nm for standard devices and 96 nm, 61 nm and 40 nm for inverted structure **PDPP[T]₂-EDOT** : PC$_{71}$BM, **PDPP[Py]₂-EDOT** : PC$_{71}$BM and **PDPP[Ph]₂-EDOT** : PC$_{71}$BM devices respectively. A 15 nm Ca layer and a 100 nm Al layer for standard structure devices or a 15 nm MoO$_x$ layer and a 100 nm Ag layer for inverted structure devices were subsequently evaporated in vacuo ($\sim 10^{-6}$ mbar) through a shadow mask to define electrodes with an active area of 4.5 mm^2. All processing steps subsequent to the weighing of solid organic semiconductor powders were conducted in a nitrogen glove box. The devices were encapsulated with epoxy resin and glass cover slides before being removed from the glove box for testing.

Device characterization

The photovoltaic characteristics of the solar cells were measured with a Keithley 2635 source measurement unit under a 1 sun, AM1.5G spectrum from a Photo Emission Tech. SS50AA solar simulator. The intensity of simulated solar light was calibrated by using a calibrated silicon solar cell with KG3 filter to obtain an accurate light intensity. External quantum efficiency (EQE) was measured as a function of wavelength by using light from a tungsten halogen lamp dispersed through a monochromator and focused onto the cell. The power density calibration was performed by placing a calibrated photodiode under test position and referencing the intensity measured to that of another silicon photodiode that samples a portion of the beam via a beam-splitter and serves to account for any intensity fluctuations.

UV-vis-NIR absorption spectroscopy was measured over the wavelength range from 300 to 1200 nm with a PerkinElmer Lambda 950 Spectrometer. Surface topography was measured with a Veeco Nanoscope V atomic force microscope (AFM) using ScanAsyst mode. TEM images were obtained using a JEOL JEM-2100F TEM operating at a voltage of 200 kV. Defocussed bright-field images were collected using a Gatan UltraScan 1000 (2k × 2k) CCD camera. A 20 μm objective aperture and a large value of defocus (−10 000 nm) were employed to increase contrast between the phases.

GIWAXS measurements. GIWAXS measurements were conducted at the SAXS/WAXS beamline of the Australian Synchrotron.[33] Samples were prepared by spin-coating films onto MoO$_x$-coated silicon wafers. Highly collimated 9 keV X-rays were calibrated to be at a tilt angle of $0 \pm 0.01°$ when parallel to the surface of each sample by use of a silicon crystal analyser. A Dectris Pilatus 1M detector collected 2D scattering patterns. Each scattering pattern was tiled together from three 1 second

3484 | J. Mater. Chem. A, 2016, **4**, 3477–3486

This journal is © The Royal Society of Chemistry 2016

images with the detector slightly moved between exposures, such that the resulting image removes gaps between the detector modules. The sample to detector distance was measured using a silver behenate scattering standard. Data was analysed using a modified version of the NIKA small angle scattering analysis package.[34]

NEXAFS spectroscopy. NEXAFS spectroscopy was performed at the soft X-ray beamline of the Australian Synchrotron[35] using a nearly perfectly linearly polarized X-ray beam. Total electron yield data was acquired by measuring the drain current flowing to the sample under X-ray illumination while partial electron yield data was acquired using a Channeltron detector with a retarding voltage of 210 V. An X-ray angle of incidence of 55° was used for all spectra. The recorded signal was normalized by the "stable monitor method",[36] with the spectra normalized by setting the pre-edge to 0 and the intensity at 320 eV to 1. NEX-AFS data were analysed with QANT.[37]

(D)   Conclusions

We have studied the photovoltaic performance and morphology of polymer solar cells based on a series of novel EDOT-containing DPP polymers. By varying the aryl flanking units on the DPP core from thiophene, to pyridine to phenyl a range of optical bandgaps spanning 1.91 to 1.13 eV was achieved, attributed to variations in backbone planarity. Despite having the lowest open circuit voltage, the thiophene flanked polymer exhibited the highest efficiency of 2.5% attributed to the more favourable morphology, crystallinity and mobility of **PDPP[T]$_2$-EDOT** : PC$_{71}$BM blends that enabled EQEs of over 50%. The performance of inverted **PDPP[T]$_2$-EDOT** : PC$_{71}$BM devices were superior to that of standard devices attributed in part to the superior optical properties of the top electrode used in the inverted structure.

Acknowledgements

References

1 C. W. Tang, US4164431 A, 1979.

2 C. W. Tang, *Appl. Phys. Lett.*, 1986, **48**, 183.

3 D. E. Markov, E. Amsterdam, P. W. M. Blom, A. B. Sieval and J. C. Hummelen, *J. Phys. Chem. A*, 2005, **109**, 5266–5274.

4 P. W. M. Blom, V. D. Mihailetchi, L. J. A. Koster and D. E. Markov, *Adv. Mater.*, 2007, **19**, 1551–1566.

5 J. J. M. Halls, C. A. Walsh, N. C. Greenham, E. A. Marseglia, R. H. Friend, S. C. Moratti and A. B. Holmes, *Nature*, 1995, **376**, 498–500.

6 G. Yu, J. Gao, J. C. Hummelen, F. Wudl and A. J. Heeger, *Science*, 1995, **270**, 1789–1791.

7 G. Yu and A. J. Heeger, *J. Appl. Phys.*, 1995, **78**, 4510.

8 Y. Liu, J. Zhao, Z. Li, C. Mu, W. Ma, H. Hu, K. Jiang, H. Lin, H. Ade and H. Yan, *Nat. Commun.*, 2014, **5**, 5293.

9 J.-D. Chen, C. Cui, Y.-Q. Li, L. Zhou, Q.-D. Ou, C. Li, Y. Li and J.-X. Tang, *Adv. Mater.*, 2015, **27**, 1035–1041.

10 S. Zhang, L. Ye, W. Zhao, B. Yang, Q. Wang and J. Hou, *Sci. China: Chem.*, 2015, **58**, 248–256.

11 M. C. Scharber, D. Mühlbacher, M. Koppe, P. Denk, C. Waldauf, A. J. Heeger and C. J. Brabec, *Adv. Mater.*, 2006, **18**, 789–794.

12 H. Zhou, L. Yang, A. C. Stuart, S. C. Price, S. Liu and W. You, *Angew. Chem., Int. Ed.*, 2011, **50**, 2995–2998.

13 P.-L. T. Boudreault, A. Najari and M. Leclerc, *Chem. Mater.*, 2011, **23**, 456–469.

14 S. Qu and H. Tian, *Chem. Commun.*, 2012, **48**, 3039–3051.

15 W. Li, Y. An, M. M. Wienk and R. A. J. Janssen, *J. Mater. Chem. A*, 2015, **3**, 6756–6760.

16 C. B. Nielsen, M. Turbiez and I. McCulloch, *Adv. Mater.*, 2013, **25**, 1859–1880.

17 K. H. Hendriks, G. H. L. Heintges, V. S. Gevaerts, M. M. Wienk and R. A. J. Janssen, *Angew. Chem., Int. Ed.*, 2013, **52**, 8341–8344.

18 J.-H. Kim, M. Lee, H. Yang and D.-H. Hwang, *J. Mater. Chem. A*, 2014, **2**, 6348–6352.

19 H. Choi, S.-J. Ko, T. Kim, P.-O. Morin, B. Walker, B. H. Lee, M. Leclerc, J. Y. Kim and A. J. Heeger, *Adv. Mater.*, 2015, **27**, 3318–3324.

20 K. H. Hendriks, W. Li, M. M. Wienk and R. A. J. Janssen, *J. Am. Chem. Soc.*, 2014, **136**, 12130–12136.

21 C. J. Mueller, C. R. Singh and M. Thelakkat, *J. Polym. Sci., Part B: Polym. Phys.*, 2016, **54**, 639–648.

22 W. Li, K. H. Hendriks, A. Furlan, W. S. C. Roelofs, M. M. Wienk and R. A. J. Janssen, *J. Am. Chem. Soc.*, 2013, **135**, 18942–18948.

23 C. R. McNeill, B. Watts, L. Thomsen, W. J. Belcher, A. K. D. Kilcoyne, N. C. Greenham and P. C. Dastoor, *Small*, 2006, **2**, 1432–1435.

24 B. A. Collins, Z. Li, J. R. Tumbleston, E. Gann, C. R. McNeill and H. Ade, *Adv. Energy Mater.*, 2013, **3**, 65–74.

25 J. J. van Franeker, M. Turbiez, W. Li, M. M. Wienk and R. A. J. Janssen, *Nat. Commun.*, 2015, **6**, 6229.

26 J. J. van Franeker, G. H. L. Heintges, C. Schaefer, G. Portale, W. Li, M. M. Wienk, P. van der Schoot and R. A. J. Janssen, *J. Am. Chem. Soc.*, 2015, **137**, 11783–11794.

27 L. A. Perez, P. Zalar, L. Ying, K. Schmidt, M. F. Toney, T.-Q. Nguyen, G. C. Bazan and E. J. Kramer, *Macromolecules*, 2014, **47**, 1403–1410.

This journal is © The Royal Society of Chemistry 2016

J. Mater. Chem. A, 2016, **4**, 3477–3486 | **3485**

28 L.-L. Chua, M. Dipankar, S. Sivaramakrishnan, X. Gao, D. Qi, A. T. S. Wee and P. K. H. Ho, *Langmuir*, 2006, **22**, 8587–8594.

29 J. Stöhr, *NEXAFS Spectroscopy*, Springer, Berlin, 1992.

30 Z. Zeng, Y. Li, J. Deng, Q. Huang and Q. Peng, *J. Mater. Chem. A*, 2014, **2**, 653–662.

31 S. Esiner, T. Bus, M. M. Wienk, K. Hermans and R. A. J. Janssen, *Adv. Energy Mater.*, 2013, **3**, 1013–1017.

32 A. K. Pandey, P. E. Shaw, I. D. W. Samuel and J.-M. Nunzi, *Appl. Phys. Lett.*, 2009, **94**, 103303.

33 N. M. Kirby, S. T. Mudie, A. M. Hawley, D. J. Cookson, H. D. T. Mertens, N. Cowieson and V. Samardzic-Boban, *J. Appl. Crystallogr.*, 2013, **46**, 1670–1680.

34 I. Ilavsky, *J. Appl. Crystallogr.*, 2012, **45**, 324–328.

35 B. C. C. Cowie, A. Tadich and L. Thomsen, *AIP Conf. Proc.*, 2010, **1234**, 307–310.

36 B. Watts, L. Thomsen and P. C. Dastoor, *J. Electron Spectrosc. Relat. Phenom.*, 2006, **151**, 105–120.

37 E. Gann, C. R. McNeill, A. Tadich, B. C. C. Cowie and L. Thomsen, *J. Synchrotron Radiat.*, 2016, **23**, 374–380.